Journal of Electronics and Electrical Engineering
https://ojs.wiserpub.com/index.php/JEEE/

UNIVERSAL WISER PUBLISHER

Research Article

Role of Phonon Scattering on the Transport and Performance of an N-Channel Monolayer Black Phosphorus Transistor

Khairul Alam

Department of Electrical and Electronic Engineering, East West University, Dhaka, Bangladesh
E-mail: kalam@ewubd.edu

Received: 5 November 2023; **Revised:** 7 December 2023; **Accepted:** 21 December 2023

Abstract: We investigate the influence of phonon scattering on the transport properties and performance metrics of a monolayer n-channel black phosphorus transistor within a four-band tight binding Hamiltonian, employing a recursive Green's function algorithm and Buttiker probe scattering model. Our analysis reveals that electron-phonon scattering significantly degrades the on-state current, while its effects in the subthreshold region are found to be negligible. Further examination identifies optical phonons as the primary contributors to the degradation of on-state current, with acoustic phonons playing a less prominent role. The ballisticity of the device declines from 42% to 24% when transitioning from solely acoustic phonon scattering to the combined influence of acoustic and optical phonons. Expanding the placement of Buttiker probes from beneath the gate region to cover the entire path from source to drain results in a further 48% reduction in on-state current. The on-state current exhibits a parabolic relationship with the inverse Kelvin temperature. To quantify the effects of phonon scattering on device performance, we assess the key parameters, transconductance and unity current gain frequency. Phonon scattering is observed to severely impact both the parameters. The on-state transconductance declines from its ballistic value of 24.9 mS/μm to 3.99 mS/μm when both acoustic and optical phonons are concurrently active. Similarly, the unity current gain frequency decreases from 1.18 to 0.2 THz due to phonon scattering. Additionally, our analysis reveals that approximately 7–9% of the total power dissipated within the device is attributed to phonon scattering effects, while the remainder is released through thermalization in the device's contacts. Phonon scattering is shown to induce both lattice cooling and heating, depending on the presence or absence of potential barriers. When a potential barrier exists in the channel, electrons injected from the source experience lattice cooling before the barrier region and lattice heating after crossing the barrier. Including the source and drain contact resistances in our model unveils that achieving a contact resistance value of approximately 100 Ω-μm is crucial for the effective functioning of black phosphorus devices.

***Keywords*:** phonon scattering, black phosphorus, 2D material transistor, NEGF, tight binding

1. Introduction

The proliferation of electronic devices in recent decades can be ascribed to advancements in semiconductor materials and transistor technologies. The emergence of ultra-thin two-dimensional (2D) materials has initiated a novel phase in semiconductor technology, distinguished by their extraordinarily smooth surfaces and outstanding electrical characteristics. These materials exhibit a high level of carrier mobility, a notable on/off current ratio, and negligible leakage current,

Copyright ©2024 Khairul Alam
DOI: https://doi.org/10.37256/jeee.3120243867
This is an open-access article distributed under a CC BY license
(Creative Commons Attribution 4.0 International License)
https://creativecommons.org/licenses/by/4.0/

especially in devices with short channels [1, 2, 3, 4]. Significantly, there has been considerable interest in the possible uses of 2D materials such as graphene [1, 5, 6] and transition metal dichalcogenides [3] in the field of nanoscaled transistors. Nevertheless, the domain of 2D materials extends beyond these widely recognized candidates, and a particularly noteworthy participant in this arena is monolayer and few-layer black phosphorus (BP). In recent years, BP has garnered significant attention in the academic community, with numerous studies conducted to explore its properties and applications in the field of 2D materials [7, 8, 9].

In the realm of field-effect transistors (FETs), black phosphorus has been extensively investigated in the literature [10, 11, 12, 13, 14, 15, 16, 17, 18, 19, 20, 21, 22]. Of particular significance is the pursuit of understanding the ballistic performance limits of monolayer BP FETs, which has been a focal point of studies [14, 15, 23, 24]. These investigations have unveiled intriguing insights into BP FETs' exceptional performance, notably marked by their high on-state current and impressive carrier mobility along the armchair direction, attributed to the lighter carrier mass. The superiority of BP transistors over MoS_2 transistors in armchair transport has been confirmed through a comparative investigation of their current-voltage (I-V) properties and carrier mobility [16]. The research conducted by Li et al. [24] has made significant contributions to the knowledge and comprehension of BP FETs, specifically focusing on the interface engineering and strategic alignment of the channel in the armchair direction. This technique has demonstrated the potential to achieve an impressive on-state current of approximately 1.6 mA/μm.

The examination of transport properties in black phosphorus transistors heavily relies on the analysis of electron-phonon scattering. Black phosphorus, a distinctive 2D material endowed with anisotropic attributes, necessitates in-depth examination of how electron-phonon scattering phenomena impact its electronic transport properties. Experimental insights into carrier mobility are primarily available for relatively thick multi-layered black phosphorus structures [7, 25, 26]. Although BP exhibits notably high mobility in thicker films, its mobility deteriorates substantially as the film thickness decreases to a few layers [27, 28]. The first-principle-based calculations have been employed to unveil anisotropic mobilities in monolayer BP [29]. However, it is essential to recognize that the behavior of electron-phonon scattering and carrier mobility may exhibit distinct patterns within the nanoscaled FET environment. Therefore, in order to thoroughly evaluate the possible usefulness of BP in transistor technology, it is crucial to conduct complete device simulations that include electron-phonon scattering and quantum non-equilibrium effects. Although only a few theoretical studies [16, 18, 30] have explored electron-phonon scattering in BP transistors, it is clear that this phenomenon significantly impairs device current, causing a reduction in ballisticity levels to 42% [18].

Phonon scattering, which results from the interaction between charge carriers and lattice vibrations known as phonons, is a major contributor to the degradation of performance in black phosphorus transistors and other semiconductor devices. A deep understanding of the complex interplay between carriers and phonons in black phosphorus transistors is crucial for devising strategies to mitigate their detrimental effects. In this study, we delve into the realm of electron-phonon interaction effects within BP transistors using a quantum transport simulation that employs a tight binding Hamiltonian, which has been validated against first-principle calculations. Notably, in BP transistors, the primary cause of current degradation is the influence of optical phonons. Electron-phonon scattering within an n-channel BP transistor significantly reduces its ballisticity to 24%, transconductance drops to 3.99 mS/μm from the ballistic value of 24.9 mS/μm, and the cut-off frequency is diminished to 0.2 THz from the ballistic value of 1.18 THz. The current in the on-state exhibits a precise inverse temperature relationship characterized by a second-degree polynomial. To attain optimal performance in black phosphorus transistors, it is imperative to achieve a contact resistance close to 100 Ω-μm. It's worth noting that only 7–9% of the total power loss is attributable to lattice heating. Furthermore, the spatial distribution of power density suggests that the presence of a potential barrier in the channel region contributes to both lattice cooling and heating effects.

2. Simulation approach

The monolayer black phosphorus possesses an orthorhombic crystal structure characterized by the basis vectors $\vec{a}_1 = (a, 0)$ and $\vec{a}_2 = (0, b)$, with the lattice constants a = 4.43 $\mathring{A}$ and b = 3.27 $\mathring{A}$, as reported in reference [31]. The unit cell comprises four atoms, and it is modeled by a 4 × 4 Hamiltonian obtained from the methodology described in reference [32].

This Hamiltonian has been verified against the *ab initio* outcomes. In order to conduct device simulation, it is necessary to have access to the unit cell matrix, denoted as h_j, as well as the coupling matrix between adjacent cells, denoted as $h_{j,j+1}$

$$\begin{aligned} h_j(k_y) &= \alpha_u + \beta_{u\omega} e^{ik_y b} + \beta^{\dagger}_{u\omega} e^{-ik_y b} + \beta_{u\omega f} e^{i2k_y b} + \beta^{\dagger}_{u\omega f} e^{-i2k_y b} \\ h_{j,j+1}(k_y) &= \beta_{ul} + \beta_{ulf} e^{ik_y b} + \beta_{ulb} e^{-ik_y b} \end{aligned} \tag{1}$$

In these equations, k_y represents the wave vector component aligned with the BP zigzag (y) direction, while the direction from the device's source to drain coincides with the BP armchair (x) direction. The 4 × 4 matrices α_u, β_{uw}, β_{uwf}, β_{ul}, β_{ulf}, and β_{ulb} are provided in Equations (1) to (5) of the reference [31]. The Hamiltonian of the device can be represented as a block tri-diagonal matrix, where the diagonal blocks are $H_{j,j} = h_{j,j}$, and the off-diagonal blocks are $H_{j,j+1} = h_{j,j+1}$ and $H_{j+1,j} = h^{\dagger}_{j,j+1}$.

With device Hamiltonian and potential profile V from a two-dimensional Poisson's solver we compute the retarded Green's function at energy E and wave vector k_y

$$G^R(E,k_y) = \left[EI - H(k_y) + eV - \sum\nolimits^C(E,k_y) - \sum\nolimits^R(E,k_y)\right]^{-1} \tag{2}$$

Here I is the identity matrix, e is the electronic charge, Σ^C is the source and drain contact self energies, and Σ^R is the retarded electron-phonon scattering self energy. We use Buttiker probe formalism for Σ^R. Buttiker probes are similar to the source and train contacts, except that they can not change the electron number in the device, although they can change energy and momentum of the carriers. This guarantees current conservation in the device [33]. Conventionally, a Buttiker probe is modeled by a coupling parameter and the probe Fermi potential, where the coupling parameter is determined from the carrier mobility [33]. In this approach, the different scattering mechanisms can not be separated, rather they are lumped into the coupling parameter. Peter Greck and coworkers [34, 35] define Σ^R in a way where different scattering mechanisms can be separated. Later, Vaitkus and Cole [36] conducted a more in-depth examination and employed this technique to investigate the electron-phonon scattering in graphene devices.

Following their approach, we define Σ^R for the acoustic and optical phonon scattering as follows

$$\sum\nolimits^R(E,k_y) = -im\left[\frac{\pi D_{AC}^2 k_B T}{\rho v_s^2} g_d(E,k_y) + \frac{\pi\hbar^2 D_{OP}^2}{2\rho\hbar\omega_0}\left[n_B g_d(E+\hbar\omega_0,k_y) + (n_B+1) g_d(E-\hbar\omega_0,k_y)\right]\right] \tag{3}$$

Here D_{AC} and D_{OP} are respectively the acoustic and optical phonon coupling strength, $k_B T$ is the thermal energy, $\hbar$ is the reduced Planck's constant, v_s is the sound velocity, n_B is the Bose-Einstein distribution number, $\hbar\omega_0$ is the optical phonon energy, ρ is the material density, and the density-of-states is

$$g_d(E,k_y) = -\frac{1}{\pi\delta\Omega}\mathrm{Im}\left[\mathrm{diag}\left(G^R(E,k_y)\right)\right] \tag{4}$$

where $\delta\Omega$ is the grid volume. Equations (2) and (3) are solved self-consistently using recursive Green's function algorithm [37, 38]. In our approach, Σ^R is a diagonal matrix.

The distribution function of a Buttiker probe p is defined by a linear combination of the distribution functions of source and drain [34]

$$f_p(E) = c_p f_s(E) + (1-c_p) f_d(E) = f_d(E) + c_p\left[f_s(E) - f_d(E)\right] \tag{5}$$

where c_p is a constant to be determined by setting the probe current to zero

$$\frac{2e}{\hbar}\sum_{k_y}\int\frac{dE}{2\pi}\mathrm{tr}\{\Gamma_p f_p A + i\Gamma_p G^<\} = 0 \tag{6}$$

Here A is the spectral function, Γ_p is the broadening function of probe p, and $G^<$ is the lesser than Green's function. On the left side we dropped the arguments for compactness. Although c_p is independent of energy and momentum, it depends on the position. Expanding the term inside the integral we get a linear system of equations like $[M]\{C\} = \{b\}$ where M is a matrix, $C = \{c_1, c_2, ..., c_{N-1}, c_N\}$ is the unknown vector and b is the right hand side vector. The diagonal elements of M matrix are

$$M_{p,p} = \frac{2e}{\hbar}\sum_{k_y}\int\frac{dE}{2\pi}\left(T_{ps} + T_{pd} + \sum_{q=1}^{N} T_{pq} - T_{pp}\right)(f_s - f_d) \tag{7}$$

and the off-diagonal elements are

$$M_{p,q} = -\frac{2e}{\hbar}\sum_{k_y}\int\frac{dE}{2\pi} T_{pq}(f_s - f_d) \tag{8}$$

The elements of the right hand side vector b are

$$b_p = \frac{2e}{\hbar}\sum_{k_y}\int\frac{dE}{2\pi} T_{ps}(f_s - f_d) \tag{9}$$

The transmission coefficient between two probes or between a probe and a contact is defined as

$$T_{pq} = \mathrm{tr}\{\Gamma_p G^R \Gamma_q G^A\} \tag{10}$$

The transmission matrix calculation requires all the blocks of G^R. To avoid the full matrix inversion, we calculate the left connected Green's function, g^L, as well (see Equations (26) and (27) of reference [39]). With the diagonal blocks of G^R and right connected Green's function g^R from the self-consistent calculation of Equations (2) and (3) and the computed left connected Green's function g^L, we pick up any diagonal block $G^R{}_{j,j}$ and walk up and down to generate the off-diagonal blocks of G^R

$$\begin{aligned} G^R_{i,j} &= g^R_{i,i} H_{i,i-1} G^R_{i-1,j} \quad \text{for } i > j \\ G^R_{i,j} &= g^L_{i,i} H_{i,i+1} G^R_{i+1,j} \quad \text{for } i < j \end{aligned} \tag{11}$$

Finally, the electron density and source lead current is computed as follows

$$n(x,z) = \sum_{k_y}\int\frac{dE}{2\pi}\mathrm{diag}\left(-iG^<(E,k_y)\right) = \sum_{k_y}\int\frac{dE}{2\pi}\mathrm{diag}\left(f_s A_s + f_d A_d + \sum_{p=1}^{N} f_p A_p\right) \tag{12}$$

$$I_S = \frac{2e}{\hbar}\sum_{k_y}\int\frac{dE}{2\pi}\left(T_{sd}(f_s - f_d) + \sum_{p=1}^{N} T_{sp}(f_s - f_p)\right) \tag{13}$$

where $A_p = G^R \Gamma_p G^{R\dagger}$ is the spectral function of probe p.

The iterative process involving the interplay between potential and charge density commences with an initial estimate of the potential profile. The commencement of the inner self-consistent loop for retarded Green's function G^R, Buttiker probe self energy Σ^R, and probe weighting factor C occurs with the potential profile. After achieving convergence in the inner loop for all energy and wave vector grids, the charge density is computed, followed by the solution of Poisson's equation in the outer loop. This represents a single iteration of the two nested loops, which persists until the outer loop reaches convergence. Subsequently, the lead current is computed and the subsequent bias point is initiated. The outer loop employs Anderson mixing [40] as a means to enhance the convergence rate of the potential profile. The outer loop exhibits convergence within a range of 6 to 10 iterations. No mixing was employed in the inner loop. The convergence criterion for the inner loop was defined as the relative change in the total density-of-states, obtained through integration over energy and wave vector, being less than 10^{-5}. The inner loop requires approximately 12 to 16 iterations to reach convergence. In

order to perform energy and reciprocal space integration, uniformly spaced grids are employed, where the energy spacing ΔE is set to 3 meV and the reciprocal space spacing Δk is set to $0.05\pi/a$. The simulation package utilized in this study is an internally developed code, implemented using the open source programming language Julia [41].

3. Results and discussions

The device employed for simulation is a BP monolayer double gate MOSFET. The device possesses a channel length L_G of 15 nm, an oxide thickness t_{ox} of 2.15 nm, a source extension L_S of 20 nm, and a drain extension L_D of 25 nm. The channel is intrinsic and both the source and drain are *n*-type doped. HfO_2, which has a dielectric constant of 19, is the gate oxide. Figure 1a depicts a cross-section of the device. The depiction of Buttiker probe scattering is illustrated in Figure 1b. The circles in this diagram indicate the BP unit cells that interact with the Buttiker probes via acoustic and optical phonon scattering. In the proposed methodology, every individual unit cell under the gate region is intricately linked to a Buttiker probe. The phenomenon of acoustic phonon scattering is facilitated by the utilization of an acoustic deformation potential with a value of 8.31 electron volts (eV), a sound velocity of 6.6×10^3 meters per second (m/s), and a material density of 1.39×10^{-7} grams per square centimeter (g/cm^2) [18, 42]. In the context of optical phonon scattering, three optical branches are employed, which are characterized by optical deformation potential values of 80.7, 66.0, and 66.0 eV/nm, accompanied by their respective phonon energies of 42.1, 51.9, and 55.0 meV [18, 42].

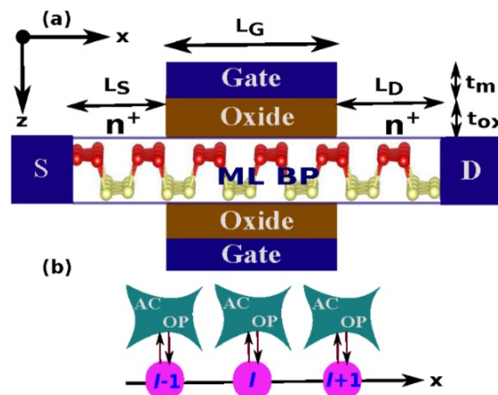

Figure 1. (**a**) The diagram illustrates a cross-section of a monolayer black phosphorus double gate metal-oxide-semiconductor field-effect transistor. The source-drain of the device is oriented in the armchair (x) direction, while the device width, which is not depicted in the cross-section, is oriented in the zigzag (y) direction. The quantization direction, denoted as z, represents the axis along which the gate voltage is applied. (**b**) The schematic depiction of Buttiker probe scattering. Pink circles represent unit cells that interact with Buttiker probes through acoustic and optical phonon scattering.

The current-voltage characteristics of ballistic and other dissipative mechanisms are depicted in Figure 2. In the context of the I-V characteristics, the gate bias V_{GS} is adjusted to a value of zero in correspondence with a source current of 5×10^{-3} µA/µm, which is commonly referred to as the off-state. The dominant scattering process, as indicated by the I-V characteristics, is the optical phonon scattering. Brahma et al. [18] also observed that the primary cause of on-state current degradation in black phosphorus n-channel MOSFETs is the optical phonon. The current in the on-state, $V_{GS} = 0.4$V, under various scattering processes is seen to be as follows: 1966 µA/µm for ballistic transport, 824 µA/µm for acoustic phonon scattering, 543 µA/µm for optical phonon scattering, and 462 µA/µm when both scattering mechanisms are simultaneously present. If we determine ballisticity based on the ratio of dissipative to ballistic drain current, then the resultant ballisticity becomes 42% for acoustic phonon scattering, 28% for optical phonon scattering, and 24% when both scattering mechanisms are active at the same time. For a 10 nm gate length BP nMOSFET, a 42% ballisticity is reported in [18]. The on-state current is greatly degraded by the larger values of deformation potential associated with the optical branches. The principal factor contributing to the present state of degradation is associated with the initial optical branch, which is defined by a D_{OP} value of 80.7 eV/nm and $\hbar\omega$ value of 42.1 meV. The carrier back scattering process is facilitated

by the initial phonon branch's strong deformation potential and low phonon energy, enabling both phonon emission and absorption. However, the subthreshold behavior is not affected by the phonon scattering process. The I-V characteristics demonstrate a subthreshold slope of 62 mV/dec.

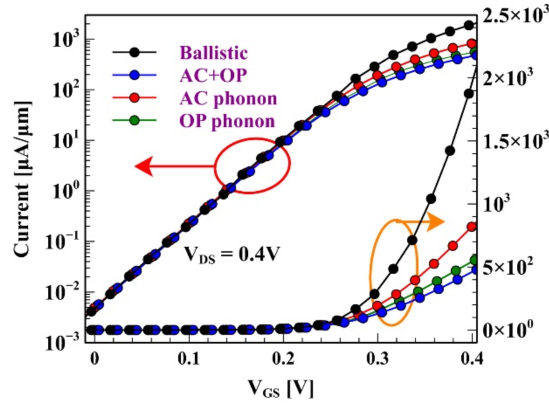

Figure 2. The current-voltage characteristics of the double gate MOSFET employed in our simulation. The transport mechanisms include ballistic transport, acoustic phonon scattering, optical phonon scattering (comprising three branches), and the combined impact of acoustic and optical phonon scattering.

To gain insight into the underlying physics of current flow mechanisms and electron energy relaxation, we have illustrated the conduction band diagrams for both the off-state and on-state, along with the corresponding source and drain current profiles, J_S and J_D respectively, in Figure 3. In the on-state, the source conduction band, E_{CS}, is positioned at −0.048 eV, whereas in the off-state, it resides at −0.032 eV, with the conduction band apex situated at 0.28 eV. The source and drain Fermi levels are $\mu_S = 0$ and $\mu_D = -0.4$ eV.

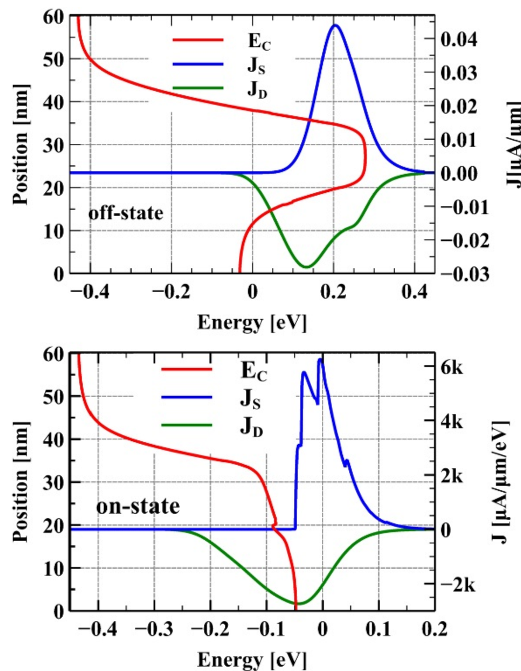

Figure 3. Plots displaying conduction band profiles and energy spectra of source and drain currents in both the off-state (VGS = 0) and on-state (VGS = 0.4V).

The currents that flow from the source and from the drain exhibit equal magnitudes, although their energy distributions differ significantly in the on-state. The injection of current from the source lead into the device occurs within the energy window $E_{CS} < E < \mu_S + 5k\text{T}$ in the on-state. In the off-state, this energy window is extended to $E_{CS} < E < \mu_S + 15k\text{T}$. This energy window is solely governed by the characteristics of the source lead [43].

When electrons are injected, they undergo energy relaxation by emitting phonons and subsequently occupy states with progressively lower energies, each reduced by the energy of a phonon, $\hbar\omega$. As electrons undergo relaxation in energy, they also tunnel out into the drain lead. The occupation of energy levels below E_{CS} is determined by the ratio between the rate of phonon relaxation and the rate of tunneling into the drain lead [43]. The presence of a considerably high magnitude of on-state drain current spectrum below E_{CS} provides strong evidence for the occurrence of many phonon scattering in the on-state.

In the hypothetical scenario when phonon scattering is not present, the value of J_D below the energy E_{CS} would be zero. Furthermore, both J_S and J_D would look similar but have the opposite sign. The off-state current spectra closely resemble this scenario, indicating that phonon scattering exerts negligible influence on the off-state currents. This is further supported by the I-V characteristics presented in Figure 2, where phonon scattering is minimal in the subthreshold region but becomes prominent in the on-state.

The characteristics of the distribution functions of the Buttiker probes also undergo considerable variations across the gate bias range. Figure 4 illustrates the weight factors associated with these probe distribution functions. In our simulation, we have considered 136 BP unit cells in the transport direction, with unit cells 45 to 81 positioned beneath the gate region. Consequently, the plotted data encompasses unit cells ranging from 45 to 81.

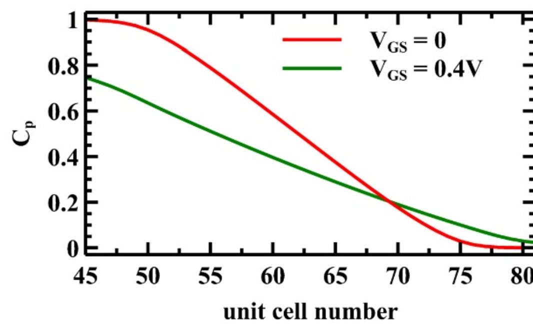

Figure 4. Graphs illustrating the weight factors of Buttiker probes' distribution functions in both the off-state and on-state.

Under lower biases, the system operates in a state of near equilibrium. Consequently, the probes located close to the source adhere to the source Fermi distribution (C_p = 1), while the probes near the drain adhere to the drain Fermi distribution (C_p = 0), as illustrated for V_{GS} = 0. When the gate bias is at zero, the initial and final probes exhibit C_p values of 1 or 0, respectively. Meanwhile, the probes positioned in the middle of the gate region manifest distribution functions as weighted averages of both the source and drain Fermi functions.

However, when the system is in the on-state, with V_{GS} = 0.4V, it operates far from equilibrium, causing the probe distribution functions to significantly deviate from the equilibrium source and drain distribution functions. Now, the distribution function of each probe represents a weighted combination of the two equilibrium source and drain distribution functions. Even the first probe nearest to the source lead exhibits a mixture with a 22% contribution from the drain Fermi function.

The transconductance, denoted by g_m, and the unity current gain frequency, denoted by f_T, of a MOSFET are key parameters for designing and optimizing electronic circuits for various applications, such as radio frequency amplifiers, analog signal processing, and high-frequency communication systems. g_m defines the correlation between the input voltage and the output current of a MOSFET, whereas f_T is the frequency at which the current amplification of a MOSFET is equal to one. While the gain of an amplifier is determined by g_m, the upper operating frequency limit of the MOSFET

as an amplifier is provided by f_T. Greater values of both parameters indicate that the MOSFET is capable of effectively amplifying signals at higher frequencies.

To determine the values of g_m and f_T, we employ the following calculations

$$\begin{aligned} g_m &= \frac{\partial i_D}{\partial v_{GS}} \Big|_{V_{DS}} \\ f_T &= \frac{g_m}{2\pi C_{gs}} \end{aligned} \tag{14}$$

Here C_{gs} is the gate-source capacitance, which is calculated as $C_{gs} = \partial Q_{ch}/\partial v_{GS}$, where Q_{ch} is the channel charge. It is important to emphasize that parasitic capacitances are not considered in this equation. Hence, f_T represents the intrinsic cut-off frequency. Nonetheless, the intrinsic f_T provides a valuable insight into how phonon scattering affects it.

The calculated g_m and f_T are shown in Figures 5 and 6, respectively. Again, it is evident from these plots that phonon scattering severely degrades both the transconductance and the cut-off frequency like the drain current. When only the acoustic phonon scattering is active, the on-state transconductance degrades from its ballistic value of 24.9 mS/μm to 7.7 mS/μm. When acoustic and optical phonon are simultaneously activated the gm value drops to 3.99 mS/μm. Similar effects are observed on cut-off frequency as well. The f_T value drops from its ballistic value of 1.18 THz to 0.2 THz when both phonon scattering mechanisms are active.

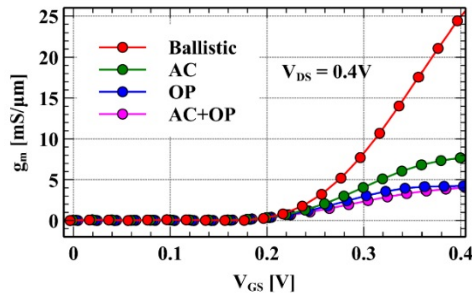

Figure 5. Plots of transconductance for various scattering mechanisms.

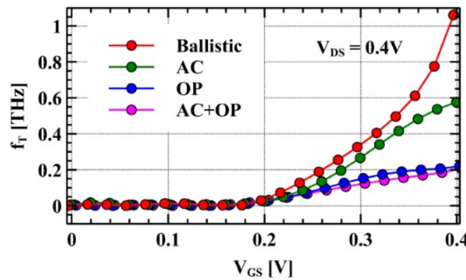

Figure 6. Plots of unity current gain frequency for various scattering mechanisms.

Power dissipation resulting from electron-phonon scattering is another significant determinant of MOSFET performance. As electrons traverse the channel of a MOSFET and encounter lattice vibrations, energy is exchanged between them and the lattice, leading to the generation of heat. The difference in the energy current flowing into and out of the two contacts represents the power dissipation in the device caused by electron-phonon interactions [43]

$$P_d = \sum_{k_y} \int \frac{dE}{2\pi\hbar} E \,\mathrm{tr}\left[\Gamma^B_{1,1}\left(f_L A_{1,1} + iG^<_{1,1}\right) + \Gamma^B_{N,N}\left(f_R A_{N,N} + iG^<_{N,N}\right)\right] \tag{15}$$

Since we already have all of the necessary matrices from the self-consistent computations, we can effortlessly calculate P_d. Figure 7 displays the power dissipation, P_d, in the device as well as the total power, VI. P_d accounts for only 7–9% of the overall power. Electrons are injected from the left lead, interact with the phonon bath in the channel area, and subsequently exit the device central part. The departing electrons possess significant energy and must achieve thermal equilibrium with the electrons of drain contact by releasing the remaining energy [43, 44].

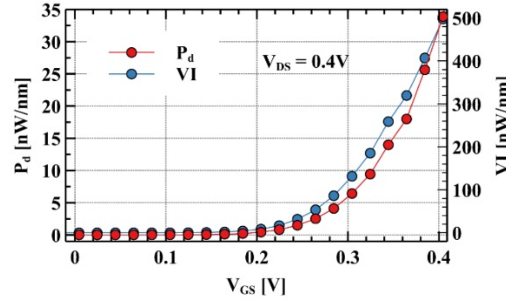

Figure 7. Graphs illustrating the device power loss due to electron-phonon scattering, along with the total power loss.

We can develop a more intuitive comprehension of power dissipation by examining the spatial distribution of power density, denoted as P_j, as illustrated in Figure 8. P_j can be calculated as [43]

$$P_j = \sum_{k_y} \int \frac{dE}{2\pi\hbar} E \left(G^<_{j,j} \Sigma^>_{j,j} - G^>_{j,j} \Sigma^<_{j,j} \right) \tag{16}$$

where j labels the unit cell. If we integrate P_j of Figure 8 from source to drain then we recover P_d of Figure 7 for the corresponding biases. The scattering centers, referred to as Buttiker probes, are positioned beneath the gate region, spanning from unit cell number 45 to 81. As the doped source region does not contain any Buttiker probes, the electrons injected from the source do not interact with the phonon bath until they reach unit cell number 45. In the off-state, there exists a substantial potential barrier of approximately 0.25 eV relative to the source Fermi level (as seen in Figure 3). Before the electrons pass through the barrier, there is a net absorption of energy from the phonon bath. During this segment, P_j is negative, signifying a cooling effect on the lattice [43, 44]. After the electrons have across the barrier, they relax by returning energy to the phonon bath and then reach a state of equilibrium with the drain contact. In the gate region beyond the potential barrier, P_j takes on a positive value, signaling a heating effect on the lattice. During the on-state, the potential is lower than the source Fermi level, as shown in Figure 3. Consequently, there is no cooling of the lattice, and P_j remains positive throughout the gate region.

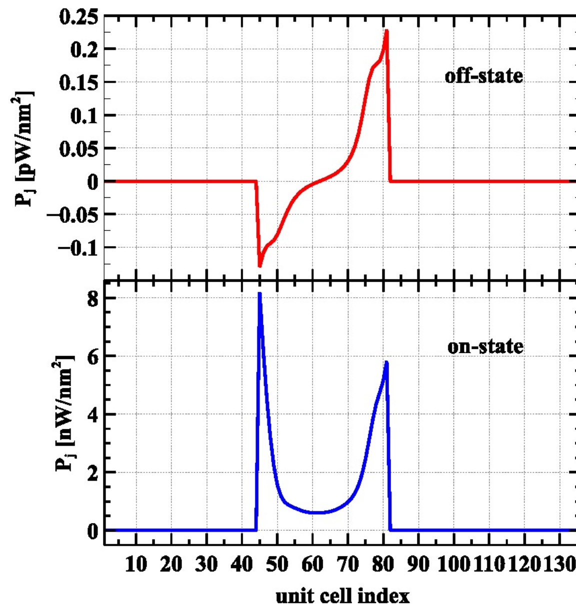

Figure 8. Plots showing spatial distribution of device power density in both the off-state and on-state.

Temperature fluctuation is a crucial factor in modern electronic devices and it has profound influence on the I-V characteristics of a transistor. Recently, Kumar et al. [45] and Yan et al. [46] investigated the temperature-dependent transport and memory behavior of a BP FET. Kumar et al. reported a decline in mobility from 283 to 33 cm^2/V-s as the temperature rises from 150 to 340 Kelvin. The heightened temperatures activate lattice vibrations (phonons), enhancing interactions with charge carriers in the semiconductor material and causing a deterioration in device current [46]. This effect is evident in Figure 9, where elevated temperature influences not only the on-state current but also the entire bias range of the I-V characteristics. Specifically, the on-state current of the device undergoes variations, decreasing from 689 μA/μm at 250 Kelvin to 462 μA/μm at 300 Kelvin and further dropping to 281 μA/μm at 350 Kelvin with changing temperatures. Figure 10 illustrates that the on-state current aligns most accurately with a second-order polynomial expansion of the inverse Kelvin temperature. Conventionally, the temperature dependence of the on-state current is typically modeled using a power law proportional to $T^{-\gamma}$. In our analysis, the best fit is achieved with a value of γ equal to 2.635. In a study by Yan et al. [46] focusing on a long-channel back-gated black phosphorus field-effect transistor, the best fit for their measured phonon scattering-limited on-state current was reported with a γ value of 2.4.

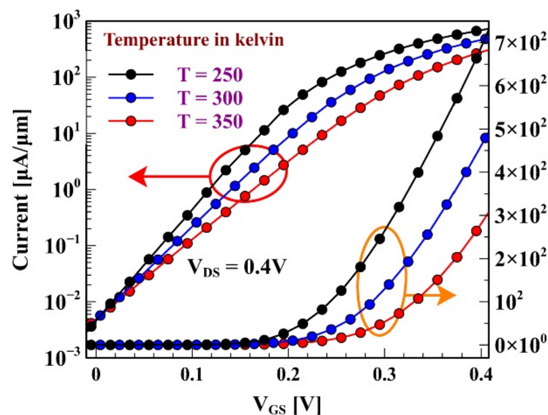

Figure 9. Plots showing I-V characteristics at different temperatures.

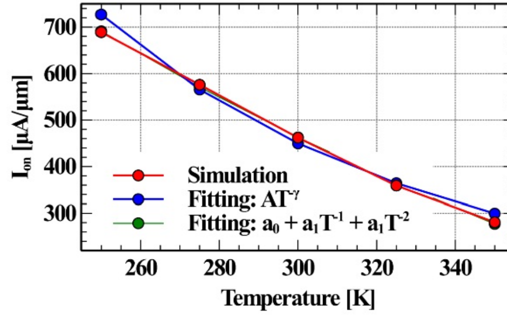

Figure 10. Plots depicting the relationship between on-state current and Kelvin temperature.

Next, we examine how the number of Buttiker probes influences the device I-V characteristics. The previously presented findings solely consider scattering under the gate region. In Figure 11 the I-V characteristics are depicted under three different conditions: (1) Buttiker probes exclusively placed beneath the gate region, (2) Buttiker probes extended halfway towards the source and drain regions, and (3) Buttiker probes positioned at every individual unit cell, including the source and drain regions. Once again, it is evident that the subthreshold region remains unaffected by an increased number of scattering centers. However, the enhanced presence of probes adversely impacts the above-threshold characteristics, particularly the on-state current. The on-state current diminishes from 462 to 297 μA/μm when the probes extend halfway towards the source and drain regions. Furthermore, the current is further reduced to 237 μA/μm when the probes cover the entire device.

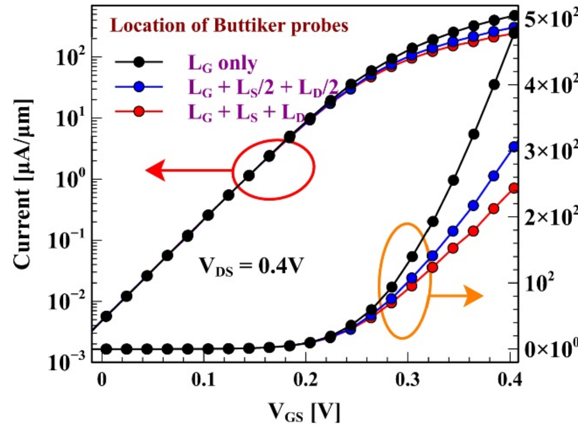

Figure 11. Plots showing I-V characteristics for different number of Buttiker probes.

Finally, we include the external part of the device, that is, the source and drain contact resistances, R_C. In this regard, the current is computed during each iteration of the outer loop, and the contact resistance drop is subtracted from V_{DS}. The modified V_{DS} is then employed as the boundary condition for the intrinsic part of the device. Notably, reported contact resistance values in literature span from approximately 100 Ω-μm to a few kΩ-μm [47, 48, 49, 50]. Additionally, a theoretical upper limit of 14 Ω-μm has been predicted [51]. At room temperature, the promising contact resistance values from [49] include 135 Ω-μm for Ni contact, 217 Ω-μm for Ti contact, and 797 Ω-μm for Cr contact. Although the highest R_C of 797 Ω-μm is considerable, the other two values align closely with the target value of the International Technology Roadmap for Semiconductors (ITRS) [52]. In Figure 12, we depict the I-V characteristics incorporating these two R_C values along with $R_C = 0$. The impact of R_C is particularly pronounced in the on-state, while the subthreshold and near-threshold behaviors remain unaffected. Specifically, the on-state current declines from 462 μA/μm to 336 μA/μm as R_C shifts from 0 to 135 Ω-μm, further decreasing to 301 μA/μm when the contact resistance rises to 217 Ω-μm.

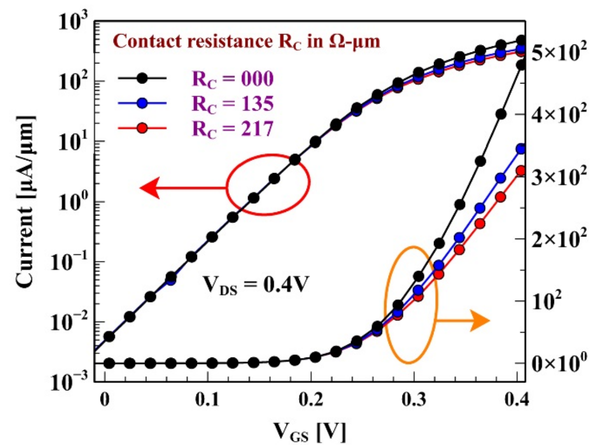

Figure 12. Plots showing I-V characteristics for different values of contact resistance.

4. Conclusions

In conclusion, we have determined that electron-phonon scattering exerts a significant impact on the on-state current, with optical phonons playing a more prominent role in degrading device performance compared to acoustic phonons. Furthermore, a precise parabolic relationship exists between the on-state current and the inverse Kelvin temperature. Phonon scattering results in a significant decline in device's ballisticity and performance metrics. Our analysis also points to the fact that a small portion of the total power is dissipated within the device due to phonon scattering, while the remainder is released through thermalization in the device's contacts. To ensure the efficient operation of black phosphorus devices, it is crucial to attain a contact resistance value of around 100 Ω-μm. In brief, our findings underscore the pivotal role of phonon scattering in shaping the performance of black phosphorus transistors, bearing implications for the design and optimization of such devices. Including additional scattering mechanisms, accounting for interface trapped charges, and providing a more accurate representation of the contacts will enhance the meaningful comparison of simulation results with experimental data and enable the derivation of design guidelines—a focus we highlight as a future extension of our work.

Conflict of interest

There is no conflict of interest for this study.

References

[1] M. Zoghi, A. Y. Goharrizi, and M. Saremi, "Band Gap Tuning of Armchair Graphene Nanoribbons by Using Antidotes," *J. Electron. Mater.*, vol. 46, pp. 340–346, 2016, https://doi.org/10.1007/s11664-016-4940-4.

[2] F. -F. Zhu et al., "Epitaxial growth of two-dimensional stanene," *Nat. Mater.*, vol. 14, pp. 1020–1025, 2015, https://doi.org/10.1038/nmat4384.

[3] B. Radisavljevic, A. Radenovic, J. Brivio, V. Giacometti, and A. Kis, "Single-layer MoS2 transistors," *Nat. Nanotechnol.*, vol. 6, pp. 147–150, 2011, https://doi.org/10.1038/nnano.2010.279.

[4] D. K. Sang, B. Wen, S. Gao, Y. Zeng, F. Meng, Z. Guo, and H. Zhang, "Electronic and Optical Properties of Two-Dimensional Tellurene: From First-Principles Calculations," *Nanomaterials*, vol. 9, p. 1075, 2019, https://doi.org/10.3390/nano9081075.

[5] A. Y. Goharrizi, M. Zoghi, and M. Saremi, "Armchair Graphene Nanoribbon Resonant Tunneling Diodes Using Antidote and BN Doping," *IEEE Trans. Electron Devices*, vol. 63, pp. 3761–3768, 2016, https://doi.org/10.1109/ted.2016.2586459.

[6] M. Saremi, M. Saremi, H. Niazi, and A. Y. Goharrizi, "Modeling of lightly doped drain and source graphene nanoribbon field effect transistors," *Superlattices Microstruct.*, vol. 60, pp. 67–72, 2013, https://doi.org/10.1016/j.spmi.2013.04.013.

[7] H. Liu et al., "Phosphorene: An Unexplored 2D Semiconductor with a High Hole Mobility," *ACS Nano*, vol. 8, pp. 4033–4041, 2014, https://doi.org/10.1021/nn501226z.

[8] A. Castellanos-Gomez et al., "Isolation and characterization of few-layer black phosphorus," *2D Mater.*, vol. 1, p. 025001, 2014, https://doi.org/10.1088/2053-1583/1/2/025001.

[9] N. Deng, H. Tian, J. Zhang, J. Jian, F. Wu, Y. Shen, Y. Yang, and T. L. Ren, "Black phosphorus junctions and their electrical and optoelectronic applications," *J. Semicond.*, vol. 42, p. 081001, 2021, https://doi.org/10.1088/1674-4926/42/8/081001.

[10] W. Li et al., "Monolayer black phosphorus and germanium arsenide transistors via van der Waals channel thinning," Nat. Electron., pp. 1–7, 2023, https://doi.org/10.1038/s41928-023-01087-8.

[11] A. Kumar et al., "Black phosphorus unipolar transistor, memory, and photodetector," *J. Mater. Sci.*, vol. 58, pp. 2689–2699, 2023, https://doi.org/10.1007/s10853-023-08169-0.

[12] Y. Zhang et al., "High-Performance Infrared Detectors Based on Black Phosphorus/Carbon Nanotube Heterojunctions," *Nanomaterials*, vol. 13, p. 2700, 2023, https://doi.org/10.3390/nano13192700.

[13] R. Wan, X. Cao, and J. Guo, "Simulation of phosphorene Schottky-barrier transistors," *Appl. Phys. Lett.*, vol. 105, p. 163511, 2014, https://doi.org/10.1063/1.4900410.

[14] K.-T. Lam, Z. Dong, and J. Guo, "Performance Limits Projection of Black Phosphorous Field-Effect Transistors," vol. 35, pp. 963–965, 2014, https://doi.org/10.1109/led.2014.2333368.

[15] F. Liu, Y. Wang, X. Liu, J. Wang, and H. Guo, "Ballistic Transport in Monolayer Black Phosphorus Transistors," *IEEE Trans. Electron Devices*, vol. 61, pp. 3871–3876, 2014, https://doi.org/10.1109/ted.2014.2353213.

[16] A. Szabo, R. Rhyner, H. Carrillo-Nunez, and M. Luisier, "Phonon-limited performance of single-layer, single-gate black phosphorus n- and p-type field-effect transistors," in *Proc. 2015 IEEE Int. Electron Devices Meeting (IEDM)*, Washington, DC, USA, 2015, pp. 12.1.1–12.1.4, https://doi.org/10.1109/IEDM.2015.7409680.

[17] T. Gao, X. Li, X. Xiong, M. Huang, T. Li, and Y. Wu, "Optimized Transport Properties in Lithium Doped Black Phosphorus Transistors," *IEEE Electron. Dev. Lett.*, vol. 39, pp. 769–772, 2018, https://doi.org/10.1109/led.2018.2820841.

[18] M. Brahma, A. Kabiraj, M. Bescond, and S. Mahapatra, "Phonon limited anisotropic quantum transport in phosphorene field effect transistors," *J. Appl. Phys.*, vol. 126, p. 114502, 2019, https://doi.org/10.1063/1.5109057.

[19] B. Das and S. Mahapatra, "A predictive model for high-frequency operation of two-dimensional transistors from first-principles," *J. Appl. Phys.*, vol. 128, p. 234502, 2020, https://doi.org/10.1063/5.0030633.

[20] B. Jiang et al., "Black phosphorus field effect transistors stable in harsh conditions via surface engineering," *Appl. Phys. Lett.*, vol. 117, p. 111602, 2020, https://doi.org/10.1063/5.0021335.

[21] R. Cheng et al., "Modulation of Negative Differential Resistance in Black Phosphorus Transistors," *Adv. Mater.*, vol. 33, p. 2008329, 2021, https://doi.org/10.1002/adma.202008329.

[22] Q. Lu et al., "Study on Black Phosphorus Characteristics Using a Two-Step Thinning Method," *Materials*, vol. 15, p. 615, 2022, https://doi.org/10.3390/ma15020615.

[23] C. Klinkert, S. Fiore, J. Backman, Y. Lee, and M. Luisier, "Impact of Orientation Misalignments on Black Phosphorus Ultrascaled Field-Effect Transistors," *IEEE Electron. Dev. Lett.*, vol. 42, pp. 434–437, 2021, https://doi.org/10.1109/LED.2021.3055287.

[24] X. Li et al., "High-speed black phosphorus field-effect transistors approaching ballistic limit," *Sci. Adv.*, vol. 5, p. eaau3194, 2019, https://doi.org/10.1126/sciadv.aau3194.

[25] F. Xia, H. Wang, and Y. Jia, "Rediscovering black phosphorus as an anisotropic layered material for optoelectronics and electronics," *Nat. Commun.*, vol. 5, p. 4458, 2014, https://doi.org/10.1038/ncomms5458.

[26] M. Lee, N. Ali, F. Ali, K. Watanabe, T. Taniguchi, and W. J. Yoo, "Ultrahigh Anisotropic Transport Properties of Black Phosphorus Field Effect Transistors Realized by Edge Contact," *Adv. Electron. Mater.*, vol. 8, p. 2100988, 2021, https://doi.org/10.1002/aelm.202100988.

[27] L. Li et al., "Black phosphorus field-effect transistors," *Nat. Nanotechnol.*, vol. 9, pp. 372–377, 2014, https://doi.org/10.1038/nnano.2014.35.

[28] R. A. Doganov, S. P. Koenig, Y. Yeo, K. Watanabe, T. Taniguchi, and B. Özyilmaz, "Transport properties of ultrathin black phosphorus on hexagonal boron nitride," *Appl. Phys. Lett.*, vol. 106, p. 083505, 2015, https://doi.org/10.1063/1.4913419.

[29] G. Gaddemane et al., "Theoretical studies of electronic transport in monolayer and bilayer phosphorene: A critical overview," *Phys. Rev. B*, vol. 98, p. 115416, 2018, https://doi.org/10.1103/PhysRevB.98.115416.

[30] G. Gaddemane, M. L. Van de Put, W. G. Vandenberghe, E. Chen, and M. V. Fischetti, "Monte Carlo analysis of phosphorene nanotransistors," *J. Comput. Electron.*, vol. 20, pp. 60–69, 2021, https://doi.org/10.1007/s10825-020-01610-6.

[31] H. Sarvari, C. Liu, A. H. Ghayour, P. Shenavar, Z. Chen, and R. Ghayour, "Atomistic quantum transport simulation of multilayer phosphorene nanoribbon field effect transistors," *Phys. E Low-Dimensional Syst. Nanostructures*, vol. 91, pp. 161–168, 2017, https://doi.org/10.1016/j.physe.2017.04.015.

[32] A. N. Rudenko, S. Yuan, and M. I. Katsnelson, "Toward a realistic description of multilayer black phosphorus: From GW approximation to large-scale tight-binding simulations," *Phys. Rev. B*, vol. 92, p. 085419, 2015, https://doi.org/10.1103/PhysRevB.92.085419.

[33] R. Venugopal, M. Paulsson, S. Goasguen, S. Datta, and M. S. Lundstrom, "A simple quantum mechanical treatment of scattering in nanoscale transistors," *J. Appl. Phys.*, vol. 93, pp. 5613–5625, 2003, https://doi.org/10.1063/1.1563298.

[34] P. Greck, "Efficient calculation of dissipative quantum transport properties in semiconductor nanostructures," Ph.D. dissertation, TU Munich, Arcisstraße, Germany, 2012.

[35] P. Greck, S. Birner, B. Huber, and P. Vogl, "Efficient method for the calculation of dissipative quantum transport in quantum cascade lasers," *Opt. Express*, vol. 23, pp. 6587–6600, 2015, https://doi.org/10.1364/OE.23.006587.

[36] J. A. Vaitkus and J. H. Cole, "Büttiker probes and the recursive Green's function: An efficient approach to include dissipation in general configurations," *Phys. Rev. B*, vol. 97, p. 085149, 2018, https://doi.org/10.1103/PhysRevB.97.085149.

[37] R. Lake, G. Klimeck, R. C. Bowen, and D. Jovanovic, "Single and multiband modeling of quantum electron transport through layered semiconductor devices," *J. Appl. Phys.*, vol. 81, pp. 7845–7869, 1997, https://doi.org/10.1063/1.365394.

[38] K. Alam, "Transport and performance study of double-walled black phosphorus nanotube transistors," *Semicond. Sci. Technol.*, vol. 37, p. 085003, 2022, https://doi.org/10.1088/1361-6641/ac773e.

[39] A. Svizhenko, M. P. Anantram, T. R. Govindan, B. Biegel, and R. Venugopal, "Two-dimensional quantum mechanical modeling of nanotransistors," *J. Appl. Phys.*, vol. 91, pp. 2343–2354, 2002, https://doi.org/10.1063/1.1432117.

[40] H. Wang, G. Wang, Q. Huang, and S. Chang, "Accelerated solution of Poisson-Schrodinger equations in nanoscale devices by Anderson mixing scheme," *Micro Nano Lett.*, vol. 4, pp. 122–127, 2009, https://doi.org/10.1049/mnl.2009.0032.

[41] J. Bezanson, A. Edelman, S. Karpinski, and V. B. Shah, "Julia: A fresh approach to numerical computing," *SIAM Rev.*, vol. 59, pp. 65–98, 2017, https://doi.org/10.1137/141000671.

[42] M. Elahi and M. Pourfath, "Ab initio effective deformation potentials of phosphorene and consistency checks," *J. Phys. Condens. Matter*, vol. 30, p. 225701, 2018, https://doi.org/10.1088/1361-648X/aabdf4.

[43] R. Lake, "Lecture notes in Quantum Device Modeling with Non Equilibrium Green Functions," Accessed: Nov. 4, 2023. [Online]. Available: https://www.dropbox.com/s/autg2ajfpnjs3ug/.

[44] R. Lake and S. Datta, "Nonequilibrium Green's-function method applied to double-barrier resonant-tunneling diodes," *Phys. Rev. B*, vol. 45, pp. 6670–6685, 1992, https://doi.org/10.1103/PhysRevB.45.6670.

[45] A. Kumar et al., "Temperature dependent black phosphorus transistor and memory," *Nano Express*, vol. 4, p. 014001, 2023, https://doi.org/10.1088/2632-959X/acbe11.

[46] X. Yan, H. Wang, and I. S. Esqueda, "Temperature-Dependent Transport in Ultrathin Black Phosphorus Field-Effect Transistors," *Nano Lett.*, vol. 19, pp. 482–487, 2018, https://doi.org/10.1021/acs.nanolett.8b04308.

[47] F. Shi et al., "Black Phosphorus Field-Effect Transistors with Improved Contact via Localized Joule Heating," *Nanomaterials*, vol. 13, p. 2607, 2023, https://doi.org/10.3390/nano13182607.

[48] L. Viscardi et al., "Black Phosphorus Nanosheets in Field Effect Transistors with Ni and NiCr Contacts," *Phys. Status Solidi B*, vol. 260, no. 9, 2023, https://doi.org/10.1002/pssb.202200537.

[49] F. Telesio et al., "Ohmic contact engineering in few–layer black phosphorus: approaching the quantum limit," *Nanotechnology*, vol. 31, p. 334002, 2020, https://doi.org/10.1088/1361-6528/ab8cf4.

[50] N. Haratipour, S. Namgung, R. Grassi, T. Low, S.-H. Oh, and S. J. Koester, "High-Performance Black Phosphorus MOSFETs Using Crystal Orientation Control and Contact Engineering," *IEEE Electron. Dev. Lett.*, vol. 38, pp. 685–688, 2017, https://doi.org/10.1109/LED.2017.2679117.

[51] M. Poljak, M. Matić, T. Župančić, and A. Zeljko, "Lower Limits of Contact Resistance in Phosphorene Nanodevices with Edge Contacts," *Nanomaterials*, vol. 12, p. 656, 2022, https://doi.org/10.3390/nano12040656.

[52] Y. Liu et al., "Pushing the Performance Limit of Sub-100 nm Molybdenum Disulfide Transistors," *Nano Lett.*, vol. 16, no. 10, pp. 6337–6342, 2016, https://doi.org/10.1021/acs.nanolett.6b02713.